Acta Materialia 289 (2025) 120869

Contents lists available at ScienceDirect

Acta Materialia

journal homepage: www.elsevier.com/locate/actamat

Full length article

Exploring grain-resolved strain tensors and non-uniform lattice deformations with Laue 3DNDT

Camilla B. Larsen [a,*,1], Stavros Samothrakitis [a,*,1], Robin Woracek [b], Efthymios Polatidis [c], Jan Čapek [a], Manas V. Upadhyay [d], Michael Tovar [e], Søren Schmidt [f], Markus Strobl [a,g,**]

[a] Laboratory for Neutron Scattering and Imaging, PSI Center for Neutron and Muon Sciences, Forschungsstrasse 111, 5232 Villigen, PSI, Switzerland
[b] European Spallation Source ERIC, P.O. Box 176, Lund 22100, Sweden
[c] Laboratory of Technology and Strength of Materials, Department of Mechanical Engineering & Aeronautics, University of Patras, Patras, Greece
[d] Laboratoire de Mécanique des Solides (LMS), École Polytechnique, Institut Polytechnique de Paris, CNRS UMR 7649, Route de Saclay, 91128 Palaiseau, France
[e] Helmholtz-Zentrum Berlin, Department Structure and Dynamics of Energy Materials, Hahn-Meitner-Platz 1, 14109 Berlin, Germany
[f] European Spallation Source ERIC, Data Management and Software Centre, Asmussens Allé 305, 2800 Lyngby, Denmark
[g] Niels Bohr Institute, University of Copenhagen, 2100 Copenhagen, Denmark

ARTICLE INFO

Keywords:
Co-Ni-Ga ferromagnetic shape-memory alloy
Strain evolution
Laue three-dimensional neutron diffraction tomography
Neutron diffractive imaging

ABSTRACT

Oligocrystalline and polycrystalline materials often display intricate grain-resolved deformation behaviours due to grain interactions, size effects, defects, and crystalline anisotropy. Gaining a deep understanding of grain deformation mechanics is essential for optimising the performance of materials in engineering and other applications. This necessitates the development of advanced experimental and theoretical tools to accurately capture and analyse these complex behaviours. Here, Laue three-dimensional neutron diffraction tomography is introduced as a high-throughput, non-destructive method to characterise grain-resolved strain and orientation changes in an oligocrystalline Co-Ni-Ga ferromagnetic shape-memory alloy during compressive deformation. Grain-resolved strain tensors were determined for 7 out of the total 11 grains indexed with a strain resolution of approximately 10^{-3}, over an applied strain range of 0%–2%. These results were obtained across various stress steps in situ, enabling direct comparisons with single-crystal models and elasto-viscoplastic Fast Fourier Transform simulations. The study demonstrates how accurate modelling of deformation behaviour, even in the elastic regime, requires detailed knowledge of the sample microstructure. Furthermore, the results reveal non-uniform deformation mechanics within individual grains, emphasising the value of Laue 3DNDT in understanding meso-scale material behaviour.

1. Introduction

The comprehensive characterisation of microstructures in polycrystalline and oligocrystalline materials is crucial for optimising their mechanical and functional properties. Determining grain size, position, and orientation enables targeted modifications to enhance material performance. Advanced three-dimensional electron-based grain mapping techniques [1–7] provide high-resolution microstructural reconstructions but require extensive sample preparation and are inherently destructive. Conversely, non-destructive X-ray-based methods [8–18] capture grain shapes and orientations effectively and allow even submicrometre resolution [19–21]. These methods can also provide insights into grain-scale and intra-granular deformation when applied in conjunction with in situ mechanical loading [22–27].

Despite the advantages of X-ray and electron-based methods, their limited penetration depth restricts their use for larger specimens, posing challenges for studying meso-scale effects in materials. In this context, non-destructive neutron-based techniques [28–35], such as Laue three-dimensional neutron diffraction tomography (Laue 3DNDT) [33], offer a powerful alternative. Laue 3DNDT builds upon the work of Peetermans et al. [28,29], being the first to demonstrate how a broad spectrum of neutrons and full-field illumination can be used to index and map grains with high experimental efficiency. Here, we expand the capabilities of Laue 3DNDT to grain-resolved strain analysis within the elastic region. By accurately fitting grain-resolved properties in both undeformed and deformed states, we resolve not only strain tensors within individual grains associated with the elastic deformation but

* Corresponding authors.
** Correspondence to: Forschungsstrasse 111, 5232 Villigen, PSI, Switzerland .
E-mail addresses: camilla.larsen@psi.ch (C.B. Larsen), stavros.samothrakitis@psi.ch (S. Samothrakitis), markus.strobl@psi.ch (M. Strobl).
[1] These authors contributed equal to this work.

https://doi.org/10.1016/j.actamat.2025.120869
Received 24 September 2024; Received in revised form 6 January 2025; Accepted 23 February 2025
Available online 5 March 2025

also follow orientation changes induced by plastic deformation and misorientations induced by dislocation slip. Such detailed strain and orientation analyses are essential for validating and refining, for example, plasticity models and predicting materials' behaviour, coming to add to previous studies in which neutron diffraction and plasticity modelling has been used to elucidate the elastic–plastic transition in materials [36–38].

We employ Laue 3DNDT to investigate the grain-resolved strain evolution in an oligocrystalline Co-Ni-Ga sample. Co-Ni-Ga alloys [39], belonging to the Heusler alloy family with A_2BC general stoichiometry [40], are known for their unique magnetic and shape-memory properties, as well as their tuneable mechanical characteristics, making them suitable for applications in energy, sensing, and actuation [41,42]. Based on heat treatments, composition, precipitation, and addition of alloying elements, Co-Ni-Ga alloys have been found to exhibit high strength, good ductility and formability, and high corrosion resistance [43–46]. The deformation behaviour of both single-crystalline and multigrain Co-Ni-Ga alloys, under compressive or tensile stress, is an active area of research, with several studies focusing on the effect of microstructure on their mechanical properties [47–53]. As the dominant crystal structure is cubic, the deformation behaviour is highly dependent on crystallographic orientation, with single-crystalline Co-Ni-Ga displaying anisotropic elastic/plastic behaviour [47,48,50]. For example, in a study by Dadda et al. (2008) [47], investigating the pseudoelasticity and cyclic stability of Co-Ni-Ga ⟨100⟩- and ⟨123⟩-oriented single-crystals, it was demonstrated that the ⟨100⟩-oriented crystals displayed near-perfect pseudoelastic stress–strain behaviour with remarkable cyclic stability and almost no alteration in their stress–strain characteristics. In contrast, cyclic compression loading resulted in rapid accumulation of irrecoverable strains in the ⟨123⟩-oriented crystals, but after a few cycles, the samples demonstrated cyclic stability with fully recoverable transformation. Dislocation activity, detwinning, and martensite stabilisation were identified as determining factors in the evolution of pseudoelastic characteristics, with detwinning being suppressed in compression along the ⟨100⟩ orientation, while adding to the overall transformation strain in the case of the ⟨123⟩ orientation.

Due to this anisotropic deformation behaviour and orientation dependence of transformation strain observed in Co-Ni-Ga single-crystals, polycrystalline samples (especially with random grain orientation distribution) often encounter deformation constraints, resulting in premature grain boundary failure during thermo-mechanical loading. As such, many approaches have been employed to tailor the grain structure of Co-Ni-Ga samples and improve their pseudoelastic response, including preparing appropriately textured or oligocrystalline materials. Vollmer et al. (2015) [49] investigated the impact of different thermo-mechanical processing, grain size, and texture on the cyclic stability of Co-Ni-Ga alloys in four conditions: solution-annealed, bicrystalline bamboo-like, hot-rolled, and forged. The study found that both texture and grain size determine the pseudoelastic performance of the samples, however, the grain size is the dominant factor when a threshold number of grains in the sample cross section is exceeded. The hot-rolled sample had a grain size of 300 – 700 μm and a strong ⟨100⟩ texture, while the solution-annealed and forged samples had large (mm range) and small (40 – 300 μm) grains, respectively, with near-random textures. The bamboo-like sample, consisting of only two large grains with a near-⟨100⟩ orientation, exhibited a superior pseudoelastic response, similar to single-crystals, with overall good cyclic stability up to 3.5% compressive strain and fully recoverable pseudoelastic strains of up to 5%. In contrast, the solution-annealed and hot-rolled samples showed rapid permanent strain evolution in the first cycle but relatively good cyclic stability during further cycling.

In this study, we characterise the deformation behaviour of a Co-Ni-Ga sample prepared using a novel hot-extrusion technique [54,55], resulting in a homogeneous oligocrystalline microstructure with reduced grain boundary density and triple junctions. We demonstrate the efficacy of Laue 3DNDT in mapping strains, advancing the development of a high-throughput neutron technique for meso-scale material analysis. Single-crystal models and elasto-viscoplastic Fast Fourier Transform (EVPFFT) simulations [56,57] highlight the key value of the experimentally obtained detailed microstructural knowledge. The current optimisation approach, based on scarce experimental observations, underscores the need for detailed experimental information, at the grain level, and accurate models that can simulate materials' behaviour. By having comprehensive experimental data and models, it is possible to design any combination of oligocrystalline and polycrystalline aggregates with optimised functional properties, tailored to specific applications.

2. Experimental

2.1. Sample

The Co-Ni-Ga sample used in this study has a nominal composition 49Co-21Ni-30Ga (in at. %). Initially, an 80 mm long cylinder with a diameter of 8 mm was cut from the material for hot-extrusion. It was then heated and extruded at 1173 K using a 2.5 MN Müller Engineering extrusion press with a speed of 5 mm/s, with subsequent air cooling. The resulting cylinder, with a final diameter of 4 mm, was further processed into a smaller cylinder with dimensions of 15 mm × Ø 4 mm. This was subjected to solution annealing at 1433 K for 24 h, followed by furnace cooling down to 1133 K for 4 h, with the sample encapsulated in a quartz tube under an argon atmosphere. This heat-treatment process induced the formation of Co-rich ductile γ-phase precipitates (identified by EBSD [46]), located both at the grain boundaries and within the grain interiors.

A detailed microstructural characterisation, including grain size distribution, γ-phase fraction, and texture, is provided in our previous study [46]. Briefly, the γ-phase constitutes approximately 11% of the material and is distributed within the grain interiors and boundaries. The grain sizes are in the sub-millimetre to millimetre scale, with a relatively homogeneous oligocrystalline microstructure achieved through the extrusion and heat-treatment process. The specific processing steps, conducted at the Institut für Werkstoffkunde (Materials Science) of the Leibniz University Hannover, ensured a material suitable for Laue 3DNDT investigations. For this study, a smaller cylinder with dimensions of 7 mm × Ø 4 mm was prepared from the previously characterised material [46].

2.2. Laue 3DNDT measurements

Laue neutron diffraction tomographies were collected at the BER II reactor of Helmholtz-Zentrum Berlin (HZB) employing the Fast Acquisition Laue Camera for Neutrons (FALCON) [58,59]. FALCON features a forward and a back scattering detector, each measuring 41.2 × 41.2 cm^2 with a pixel size of 103 μm. The thermal neutron spectrum of the reactor was used with the full wavelength range available, $0.9 \leq \lambda \leq 3.2$ Å. The Co-Ni-Ga sample was subjected to in situ compression, with a deformation rate of 100 μm/min and stress values between 30 MPa (reference) and 610 MPa, using a specially designed transportable load-frame [60] positioned between the two detectors symmetrically (see Fig. 1), with sample-to-detector distances of 165(2) mm. The load-frame was equipped with hardened-steel grips that securely held the sample in position during compression. The stress values corresponding to the measurements taken during compression are marked on the accompanying stress–strain curve and are the focus of our analysis. For each stress step, tomographic data were collected by rotating the sample (ω-rotation about the z axis) and recording diffraction images every $\Delta\omega = 8°$ for a full 0 – 360° ω-rotation, resulting in 46 projections per tomography. Each projection was acquired with a 90 s exposure, and thus, each complete tomography was measured in about 1 h. This setup allowed for efficient and precise control of the compression conditions, facilitating the collection of high-quality tomographic data at different stress steps.

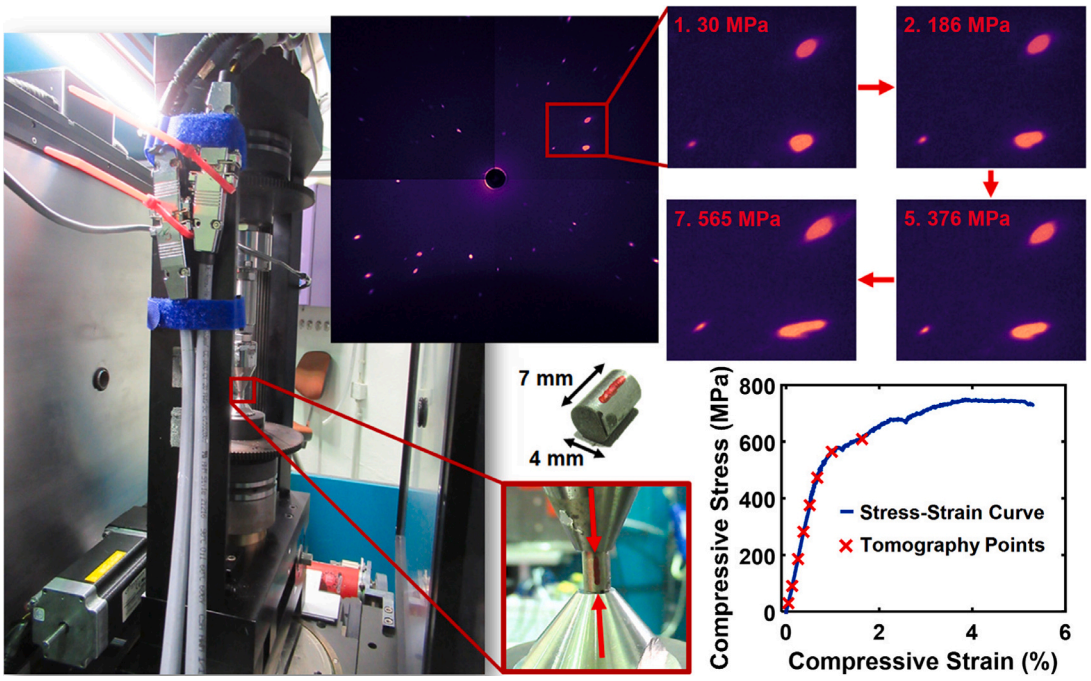

Fig. 1. Experimental setup of the in situ compressive deformation study of the Co-Ni-Ga sample, featuring the transportable load-frame, along with an example diffraction image from the forward scattering detector. The load-frame was positioned upright between the FALCON diffraction detectors, such that a compressive load was applied perpendicular to the incoming neutron beam. Insets show a magnified view of prominent diffraction spots, tracking their positional and morphological changes in response to the applied compressive stress. The lower right corner showcases the stress–strain curve obtained from the load-frame, giving an indication of the overall macroscopic response of the Co-Ni-Ga sample and depicting points at which full tomography data sets were collected.

2.3. Data indexing

Tomographic data collected at the reference stress step was indexed using the Laue 3DNDT algorithm described in Reference [33]. For the indexing, we used an $Im\bar{3}m$ space group, corresponding to the B2 austenitic phase of the Co-Ni-Ga matrix, with lattice parameters $a = b = c = 2.8657$ Å and $\alpha = \beta = \gamma = 90°$ [61]. To extract the shapes and centre-of-mass coordinates of the diffraction spots, we first applied background subtraction and noise cleaning to the raw data images [59], followed by spot segmentation/labelling. The latter step was carried out using PetroFit [62], a package based on the Photutils python package [63], which was developed for calculating Petrosian properties and fitting galaxy light profiles, and in our case proved efficient for labelling and extracting spot shapes from neutron diffraction patterns. We note that the same initial image processing was also performed for the tomographic data collected at subsequent stress steps. The Laue 3DNDT indexing procedure results in identifying individual grains in the sample, determining their orientation and centre-of-mass position. Each diffraction spot is additionally assigned a grain label and a corresponding *hkl* plane, as required for the subsequent grain-resolved strain fitting.

2.4. Single-crystal model calculations and EVPFFT simulations

The single-crystal modelling was performed by taking into account the orientation-dependent behaviour of each grain, employing the expression for the anisotropic Young's modulus for cubic crystal systems [64,65]:

$$\frac{1}{E_{hkl}} = s_{11} + \left(s_{11} - s_{12} - \frac{1}{2}s_{44}\right)\left(m^4 + n^4 + p^4 - 1\right), \quad (1)$$

where m, n, p are the direction cosines for the direction along which E_{hkl} is calculated. s_{ij} are the three independent constants of the compliance matrix, S_{hkl}, which is the inverse of the stiffness matrix, C_{hkl}. For the calculations we used the three independent stiffness matrix constants c_{11}, c_{12}, c_{44}, estimated for Co-Ni-Ga based on first principles density functional theory simulations [66], which predict a pronounced anisotropy with ⟨111⟩ and ⟨001⟩ corresponding to the least and most elastically compliant orientations, respectively.

More extensive numerical modelling, taking grain morphology and neighbourhood interactions into account, were carried out with the small deformation Elasto-Viscoplastic Fast Fourier Transform (EVPFFT) approach. This model, introduced by Lebensohn et al. [56], is a full-field approach that calculates evolving micro-mechanical fields within a voxelised sample representation using the Fast Fourier algorithm; in this work, the numerical implementation in Fortran90 developed in Ref. [57] is used. The EVPFFT model solves the periodic Lippmann Schwinger problem for an elasto-viscoplastic polycrystalline material using the augmented Lagrangian iterative scheme [67]. The elastic response is modelled using the Hooke's law and the viscoplastic response is modelled using a power law relationship between plastic strain rate and the Cauchy stress. A Voce-type isotropic hardening law is used to capture the stress–strain response during the monotonic loading studied in this work. The deformation conditions, as given by the axis of deformation and strain rate, the sample microstructure, as well as the elastic properties of the sample, were used as input parameters. For the strain rate, we used the same value as for the experiment (see above). The sample microstructure was defined from the morphology reconstruction (see Fig. 2a), given as a $64 \times 64 \times 52$ structured grid. A second phase of air voxels was introduced to envelope the cylinder in the planes with normals along $\pm x$ and $\pm y$ to simulate the effect of free surfaces. No gas voxels were added along the vertical $\pm$ z-direction in order to emulate direct contact between the load-frame grips and the sample. Elastic properties were defined through the stiffness matrix, using the same constants, c_{11}, c_{12}, c_{44}, as for the single-crystal modelling. The evolving elastic strain fields within the sample were simulated up to a maximum stress value of 611 MPa to match the experimental conditions. Comparisons with the experimentally refined values were made by calculating the average $\varepsilon_{33}^{sample}$ strains within each grain at selected stress states. Plasticity was not simulated.

3. Strain fitting method

Before strain fitting, spot assignment of data collected at subsequent stress steps is performed through correlation to previous measurements; spots are matched to indexed spots of the previous tomography, at the stress step before, based on their geometric distance. It appears generally beneficial to perform the strain analysis via many intermediate steps to track the spot movements reliably. Once the spot assignment of a deformed state is complete, strains can be extracted through a fitting routine, as is done in the monochromatic case [22]. The fitting is done based on the matrix formulation of Bragg's law [9]:

$$\Gamma^{-1}\boldsymbol{G}_{j(i)} = \frac{\lambda_{j(i)}}{4\pi}\boldsymbol{U}_i\boldsymbol{B}_i\boldsymbol{G}_{hkl,j(i)}, \tag{2}$$

where $\boldsymbol{G}_{j(i)}$ is the unrotated, experimentally determined, reciprocal scattering vector resolved from the position of the j^{th} diffraction spot of the i^{th} grain, Γ is the generalised rotation matrix describing the tomographic rotation as defined by the angle ω, $\boldsymbol{U}_i$ and $\boldsymbol{B}_i$ are the orientation matrix and reciprocal-space metric of the i^{th} grain, respectively, and $\lambda_{j(i)}$ and $\boldsymbol{G}_{hkl,j(i)} = (h,k,l)^T$ are the wavelength and hkl plane relative to a diffraction spot. In monochromatic experiments, $\lambda_{j(i)}$ is a known experimental parameter, whereas it is an implicit parameter in the white beam case. For every set of $\boldsymbol{U}_i$, $\boldsymbol{B}_i$, and $\boldsymbol{G}_{hkl,j(i)}$, $\lambda_{j(i)}$ is in Laue experiments calculated as the wavelength in the spectrum that fulfils the Bragg condition for a particular diffraction spot.

The lattice parameters of each grain i, $[a_i\ b_i\ c_i\ \alpha_i\ \beta_i\ \gamma_i]$, are fitting parameters that enter into the reciprocal-space metric, $\boldsymbol{B}_i$. The real-space equivalent, $\boldsymbol{A}_i$, can correspondingly be calculated to obtain the resulting 3D strain tensor of each grain, $\boldsymbol{\varepsilon}_i$:

$$\boldsymbol{\varepsilon}_i = \frac{1}{2}[\boldsymbol{A}_i\boldsymbol{A}_{i,0}^{-1} + (\boldsymbol{A}_i\boldsymbol{A}_{i,0}^{-1})^T] - \boldsymbol{I}, \qquad \text{with} \tag{3a}$$

$$\boldsymbol{A}_i = \begin{pmatrix} a_i & b_i\cos\gamma_i & c_i\cos\beta_i \\ 0 & b_i\sin\gamma_i & -c\sin\beta_i\cos\alpha_i^* \\ 0 & 0 & c_i\sin\beta_i\sin\alpha_i^* \end{pmatrix}, \quad \text{and} \tag{3b}$$

$$\boldsymbol{B}_i = 2\pi\cdot\begin{pmatrix} a_i^* & b_i^*\cos\gamma_i^* & c_i^*\cos\beta_i^* \\ 0 & b_i^*\sin\gamma_i^* & -c^*\sin\beta_i^*\cos\alpha_i \\ 0 & 0 & c_i^*\sin\beta_i^*\sin\alpha_i \end{pmatrix}, \tag{3c}$$

where $\boldsymbol{A}_i$ ($\boldsymbol{A}_{i,0}$) describes the correspondence between the deformed (undeformed) real-space lattice coordinate system and the Cartesian grain system, and $\boldsymbol{I}$ is the identity matrix. Fitting parameters are additionally defined in Section S1 of the Supplementary.

In the fitting routine, the differences between the experimental and theoretical scattering vectors, as defined in Eq. (2), are minimised using the Matlab `fmincon` optimiser. Detector parameters are refined from the reference measurement, assuming initial d_0 values corresponding to the undeformed lattice parameters for all grains, while starting parameters for the grain positions and orientations are obtained from the Laue 3DNDT grain indexing output. Individual tomography projection angles, ω_n, are refined from a global fit of all grains for better spot matching accuracy. Once the projection angles have been refined, the orientations and lattice parameters could be refined on a grain-by-grain basis.

Volumetric strain only affects the length of the scattering vector and hence will not affect its geometric projection onto the detector. Similar to the theoretical LabXRS procedure described in Ref. [68], we therefore enforce the constraint $\varepsilon_{11}+\varepsilon_{22}+\varepsilon_{33} = 0$, i.e., zero dilatational strain, for each grain during the fitting process to lift the inherent null space in the Bragg condition when measuring in Laue mode. Here ε_{kk} refers to diagonal elements of a grain-resolved strain tensor in the grain coordinate system as obtained from Eq. (3a). Comparisons between grains are done by comparing strain tensors transformed to the common sample coordinate system via $\boldsymbol{\varepsilon}_i^{sample} = \boldsymbol{U}_i\boldsymbol{\varepsilon}_i\boldsymbol{U}_i^T$. In the sample coordinate system, the loading direction is unequivocally for all grains along the $\hat{z}$-direction, corresponding to the $\varepsilon_{33}^{sample}$ strain tensor elements.

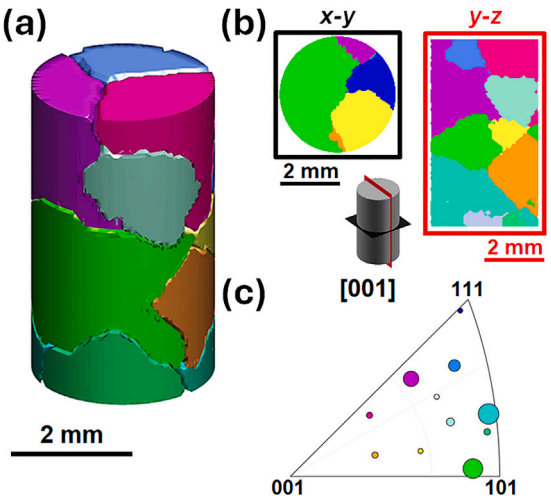

Fig. 2. Morphological map of the sample volume obtained from the indexed centre-of-mass positions in (a) isoprojection and (b) along the x-y and y-z planes, in accordance to the schematic in the figure. The relative volume of each grain is fixed to match their relative average intensity among the indexed grains. (c) Inverse pole figure (IPF) map containing the orientations of the 11 indexed grains of the Co-Ni-Ga sample, where [001] corresponds to the loading direction. The sizes of the circles reflect the relative grain-sizes, again determined from their relative average spot intensity. The grains are colour-coded according to their orientations. (For interpretation of the references to colour in this figure legend, the reader is referred to the web version of this article.)

4. Results and discussion

4.1. Indexing and grain mapping

Indexing of the reference measurement data returned a total number of 11 grains (see Fig. 2). Fig. 2a depicts the reconstructed 3D model of the grain microstructure of the Co-Ni-Ga sample in isoprojection, after a digital volume-filling operation was applied, with ortho-slices of the microstructure along the x-y and y-z planes given in Fig. 2b. For the volume-filling we used the relative volume of each grain, calculated as described in Ref. [33], as a boundary condition. The orientation distribution of the grains is given in Fig. 2c by the inverse pole figure (IPF) map, in which we see that there is no preferred crystallographic orientation. The size of each marker in the IPF was scaled based on the relative volume of each grain. Calculating the misorientation angles between the indexed grains we find that no adjacent grains have a misorientation angle less than 15 °, thus practically no low-angle grain boundaries exist in the microstructure. The above results are well in agreement with our previous study [46].

4.2. Grain-resolved strain evolution

The evaluation of the grain-resolved deformation behaviour of the Co-Ni-Ga sample focused on the evolution of the lattice strain, as expressed through the elastic strain tensors that are derived from the fits to the tomographic data, as described above. For robustness, the analysis was limited to the 7 largest grains, as the smaller ones produced dim diffraction spots that were challenging to track and fit reliably. The main strain results, obtained from all stress steps, are summarised in Fig. 3. In Figs. 3a–c, the fitted diagonal strain tensor elements in the sample coordinate system are plotted as a function of applied (nominal) stress. The errors of the fitting parameters were estimated from a Monte Carlo error propagation method, with the uncertainties of the centre-of-mass coordinates of the diffraction spots set to be 0.6 mm [59], giving strain uncertainties of $\sim 1\times10^{-3}$. Examples of fitted spot positions in comparison to experimental are shown in Figure S2 of the Supplementary. From the plots we observe a clear increase in

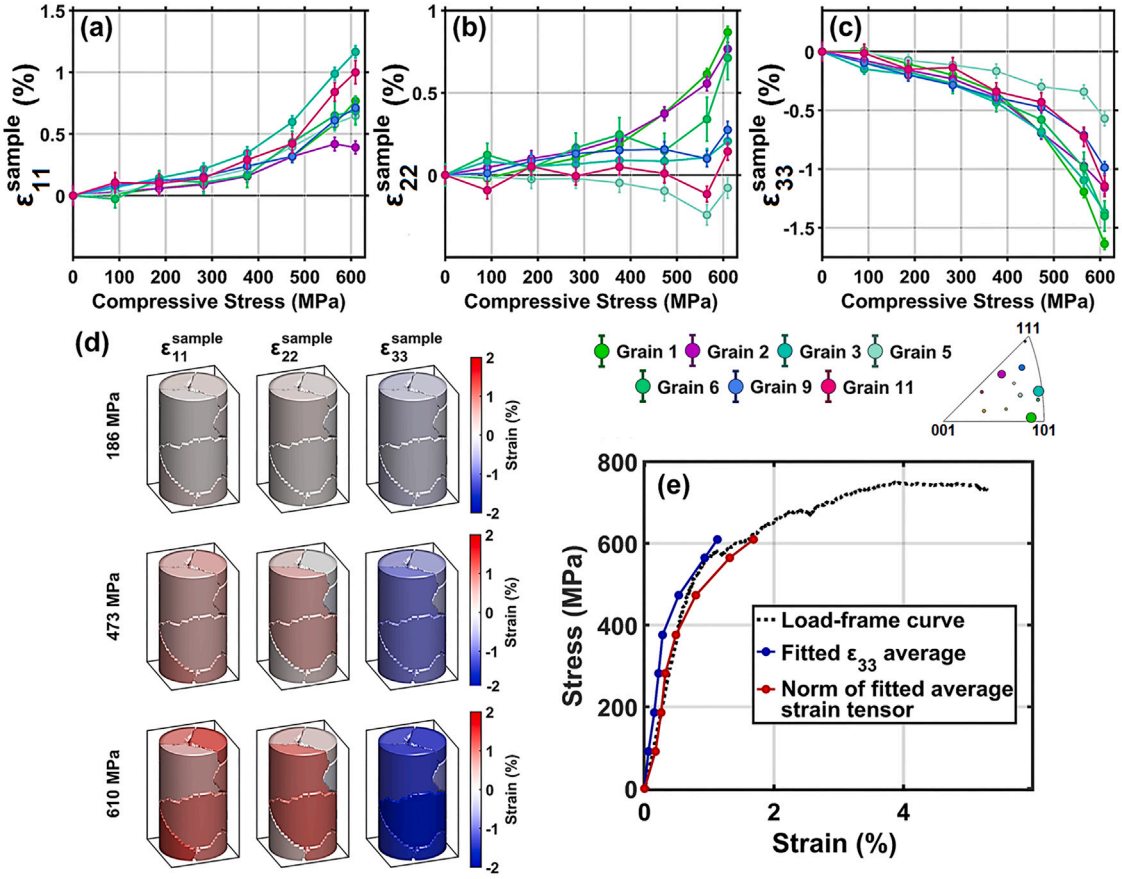

Fig. 3. (a)–(c) Evolution of the diagonal elements of the grain-resolved strain tensors in the sample coordinate reference system as a function of applied compressive stress. Each curve corresponds to a single grain and is colour-coded according to its reference state IPF colour. (d) Morphological distribution of strains in the sample. Each row corresponds to a selected stress value, while each column corresponds to a different diagonal element of the strain tensor in the sample coordinate system as input for the colour map. (e) Macroscopic deformation behaviour as depicted through the load-frame stress–strain curve, the intensity-weighted average of the $\varepsilon_{33}^{sample}$ strain tensor elements, and the intensity-weighted average of the 2-norm of the fitted strain tensors. (For interpretation of the references to colour in this figure legend, the reader is referred to the web version of this article.)

the compressive strain with increasing compressive stress in the loading direction (Fig. 3c), and conversely, an increase in tensile strains in the two orthogonal directions (Figs. 3a, b). While these plots suggest a collective response to deformation with relatively uniform elastic behaviour across the grains, some heterogeneity is evident. Specifically, in Fig. 3b, differences in strain evolution are visible among individual grains, particularly in the orthogonal directions. This variation may result from anisotropic effects, localised grain-grain interactions, grain shape effects, or differences in the γ-phase precipitate distribution, which contribute to the non-uniform deformation mechanics. The results are further illustrated by the strain tensor elements from three example tomographies superimposed on the morphological map of the sample, given in Fig. 3d. The largest grain by volume, Grain 1, located in the vertical centre of the morphological map, appears to accumulate the most negative strains, particularly in the loading direction, $\varepsilon_{33}^{sample}$. This can be partially attributed to its orientation, which is more compliant than that of the other large grains, such as Grain 2 and Grain 3. Furthermore, compared to smaller grains with the same or lower elastic modulus, large grains experience reduced mechanical constraint from surrounding grains, thus accumulating higher strains.

Fig. 3e provides a multifaceted view of the deformation behaviour by comparing the macroscopic stress–strain curve from the load-frame, the intensity-weighted average of the $\varepsilon_{33}^{sample}$ strain tensor elements, and the 2-norm of the full fitted strain tensors. The observed difference between the load-frame curve and the $\varepsilon_{33}^{sample}$ curve primarily manifests as a vertical offset, reflecting a discrepancy in strain magnitude. This offset likely arises because the load-frame captures the overall response of the material, including contributions from both normal and shear strains, while the $\varepsilon_{33}^{sample}$ tensor elements represent only the normal strain in the loading direction. The better agreement between the 2-norm of the fitted tensors and the load-frame curve supports this interpretation, as the 2-norm provides a measure of the total strain magnitude, integrating contributions from all strain components. Additionally, a potential shift in the yield point may be related to localised shear strain effects that are not fully captured by the $\varepsilon_{33}^{sample}$ curve alone. Overall, these findings highlight the complexity of interpreting macroscopic mechanical properties from microscopic strain data and underscore the importance of considering multiple strain components, grain interactions, and size effects when analysing deformation behaviour in oligocrystalline materials.

4.3. Single-crystal models & EVPFFT simulations

Fig. 4 illustrates the $\varepsilon_{33}^{sample}$ strain curves for individual grains in the elastic range and a comparison with the predictions from the single-crystal model calculations [65,66] and EVPFFT simulations [56,57]. The single-crystal model (black curves), which provides stress–strain responses based on the material's elastic constants, c_{11}, c_{12}, c_{44}, and the specific crystallographic orientation of each grain, demonstrates a clear anisotropic response aligning well with theoretical predictions [66] and observations from single-crystal experiments [47]. However, it is an infinite domain model that does not account for inter-granular interactions or boundary conditions, leading to significant differences from the experimental data, especially at higher stresses.

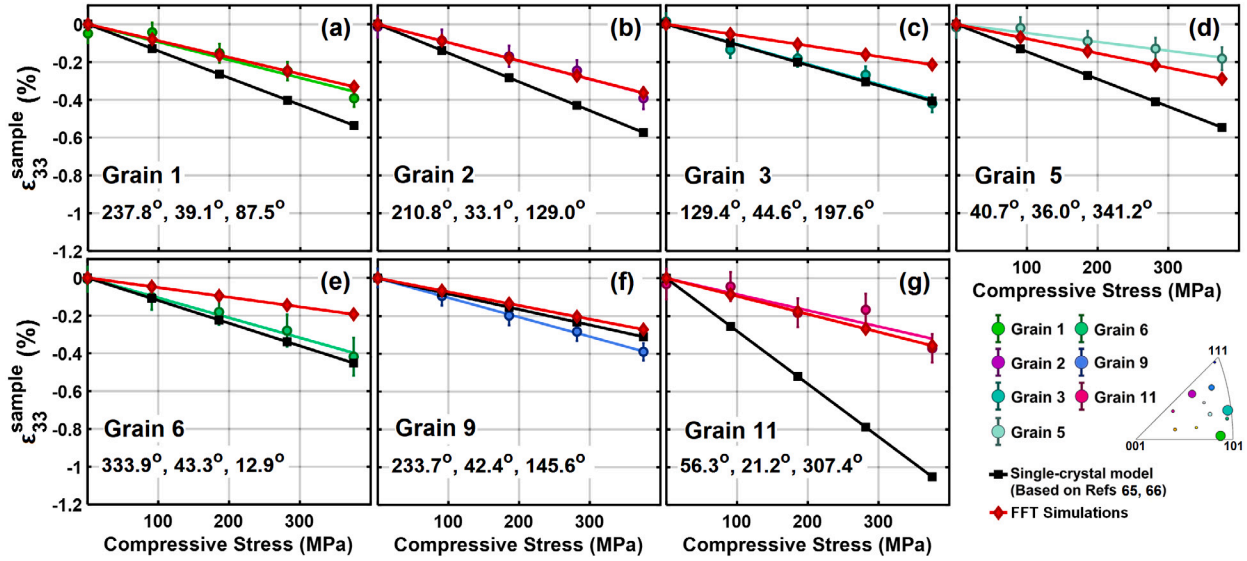

Fig. 4. (a)–(g) Comparison between the fitted strain results, calculations of strain curves as according to anisotropic single-crystal calculations, and EVPFFT simulations. Each subplot shows the behaviour of one of the 7 grains that have been used for strain-fitting. The black curves correspond to the single-crystal calculations, the red curves are the results of the EVPFFT simulations, while the remaining coloured curves represent the fitted strain values, with the specific colour corresponding to the orientation-defined IPF colourmap of the particular grain. The three angles in each panel correspond to the Euler angles, ϕ_1, Φ, ϕ_2, of each grain as fitted in the reference state. (For interpretation of the references to colour in this figure legend, the reader is referred to the web version of this article.)

The EVPFFT model (red curves) additionally incorporates the overall sample morphology, boundary conditions and grain neighbourhood (inter-granular interactions). EVPFFT simulation predictions match well with the experimental grain-averaged lattice strain data (coloured curves), effectively capturing the complex stress–strain behaviour of polycrystalline materials. Furthermore, both the experimental and EVPFFT-derived grain-averaged strain curves display significantly reduced variation, a characteristic attributable to the oligocrystalline microstructure. In this context, the relatively small number of grains leads to a heightened influence of individual grain orientations compared to polycrystalline samples. Concurrently, the grains impose mutual constraints, preventing deformation from occurring fully in accordance with single-crystal expectations. Consequently, the sample exhibits behaviour that is characteristic of oligocrystalline materials: more anisotropic than polycrystalline samples, yet less so than single crystals due to intergranular interactions.

Despite the overall agreement between diffraction and EVPFFT simulations, we see that there is deviation for some grains (e.g., grains 3, 5, and 6). Such differences are further evident when comparing the simulated ϵ_{11}^{sample} and ϵ_{22}^{sample} elements shown in the Supplementary in Figure S3 as well as in the morphological simulation output in Figure S4. The differences can be partially attributed to the limited spatial resolution of the morphological reconstruction used as input for the EVPFFT simulations. Beyond grain interactions, however, variations in stoichiometry and the emergence of extra phases also play a significant role in deformation behaviour of samples. Specifically, our observations from a previous study [46] show the presence of γ-phase precipitates within the sample. These precipitates exhibit a chemical composition distinct from that of the sample matrix, underscoring their influence on the deformation properties of the materials [69]. Differences in stoichiometry could affect the c constants of the sample, which may differ slightly from the theoretical values used for the simulations.

In light of these considerations, the findings of the present investigation indicate that the mechanical behaviour of oligocrystalline materials cannot be straightforwardly deduced from the behaviour of their single-crystal counterparts. The multifaceted nature of deformation in oligocrystalline materials necessitates a holistic approach that integrates knowledge of the microstructural characteristics and their elastic properties to predict the material's macroscopic properties. The consistency between the fitted strain data and the EVPFFT simulations underscores the efficacy of the simulation approach and highlights the importance of knowing both the sample microstructure and overall elastic constants in predicting the mechanical response of oligocrystalline materials.

4.4. Comprehensive characterisation of deformation

In addition to lattice strains, further deformation mechanics can be deduced from the Laue diffraction data. Fig. 5a shows the changing grain orientation derived from the experimental fits, indicating that all grains realign as load is applied. To improve clarity, arrows indicating the primary directions of grain reorientation are added, emphasising the directional trends of rotation. These reorientations, quantified as misorientations relative to the reference orientation in Fig. 5b, highlight a gradual increase across all grains, even in the elastic regime. This finding suggests that reversible rotations or slight realignments occur at stresses below the macroscopic yield point.

Figs. 5c and 5d depict the increasing average Full Width at Half Maximum (FWHM) of the diffraction spots in the radial and azimuthal directions, respectively, as a function of applied compressive stress. To aid in interpretation, the absolute FWHM values of the grains of the undeformed sample are given in Table S1 of the Supplementary. The observed relative increases of up to about 30% in both directions reflect the progressive introduction of heterogeneity in the strain and orientation distributions within each grain. Radial broadening is indicative of increased microstrain, which corresponds to non-uniform strain distributions within grains. Meanwhile, azimuthal broadening suggests a widening of the orientation distribution function, reflecting grain-scale lattice rotation and the evolution of misorientations. It is worth noting that these effects are compounded by the sample's inherent microstructural features. The absence of low-angle grain boundaries and the presence of γ-phase precipitates contribute to localised stress concentrations, which likely exacerbate the heterogeneous deformation behaviour. These initial conditions serve as a baseline for evaluating the observed deformation behaviour under load.

These findings emphasise the value of Laue 3DNDT in capturing not only strain but also subtle changes in orientation and crystallographic perfection, which are critical for validating micromechanical models. Incorporating such detailed information into modelling efforts, such

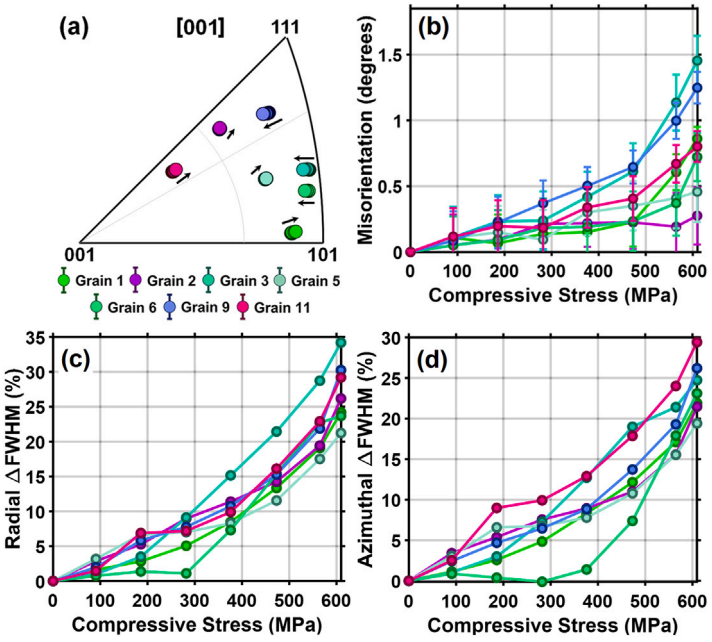

Fig. 5. (a) IPF map depicting the compression-induced reorientation of each grain at the different stress steps. The reference orientation is plotted first, while the grain orientations at higher stress value are plotted sequentially on top. The arrows indicate the orientation changes direction. (b) The misorientation of each grain with respect to the reference measurement as a function of applied compressive stress. Each curve is colour-coded according to the grain-orientation, in agreement with the IPF. (c), (d) Increase of the intensity-averaged spot widths of each grain, in terms of FWHM, measured along each spot's radial and azimuthal directions, as a function of applied compressive stress. (For interpretation of the references to colour in this figure legend, the reader is referred to the web version of this article.)

as elasto-viscoplastic Fast Fourier Transform simulations, could significantly enhance the accuracy of predictions regarding grain-scale and aggregate mechanical behaviour.

5. Conclusion

In conclusion, this study utilises Laue three-dimensional neutron diffraction tomography to non-destructively characterise grain-resolved strain tensors and orientation changes in oligocrystalline Co-Ni-Ga alloys subjected to in situ compressive stress. The analysis reveals that the average fitted strains in the loading direction agree reasonably well with macroscopic stress–strain measurements from the load-frame. Comparisons with theoretical models highlight the limitations of single-crystal predictions, which fail to replicate the observed strain responses for all grains. Elasto-viscoplastic Fast Fourier Transform simulations, incorporating theoretical elastic constants along with the measured sample microstructure, better match experimental lattice strains within the elastic regime but slightly diverge under higher stresses. This discrepancy points to the need for higher-resolution input models that more accurately represent grain boundaries and the presence of Co-rich γ-phase precipitates, which are anticipated from heat treatments but remain too small to be detectable within our resolution limit. The observed broadening of diffraction spots indicates increasingly heterogeneous strain and orientation distributions within each grain, even under low applied stresses, underscoring the impact of grain interactions and surface effects. These findings emphasise the complexity of deformation mechanics, even in samples with relatively few grains and validate the need and effectiveness of Laue 3DNDT in strain mapping. The method's efficiency, requiring less than a day of beam time, provides insights that can be used to evaluate and refine theoretical models.

Looking ahead, future developments in neutron sources and detector technologies can increase flux and strain sensitivity, facilitating shorter acquisition times and enabling the analysis of finer intragranular heterogeneities in smaller or more complex samples. Incorporating advanced data processing and machine learning algorithms will improve spot identification, strain tensor fitting, and the resolution of grain boundaries, potentially bolstered by complementary imaging techniques. Moreover, expanding the measurable strain range through improved calibration methods and in situ environmental controls will allow the study of more complex deformation mechanisms, including plasticity. These advancements will ultimately further improve our technique to deepen our understanding of the response of polycrystalline materials under a wider range of conditions.

CRediT authorship contribution statement

Camilla B. Larsen: Writing – original draft, Validation, Methodology, Investigation, Formal analysis, Data curation, Conceptualization. **Stavros Samothrakitis:** Writing – original draft, Validation, Methodology, Investigation, Formal analysis, Data curation, Conceptualization. **Robin Woracek:** Writing – review & editing, Investigation, Conceptualization. **Efthymios Polatidis:** Writing – review & editing, Formal analysis. **Jan Čapek:** Writing – review & editing, Formal analysis. **Manas V. Upadhyay:** Writing – review & editing, Validation, Methodology, Formal analysis. **Michael Tovar:** Writing – review & editing, Resources, Investigation. **Søren Schmidt:** Writing – review & editing, Supervision, Methodology. **Markus Strobl:** Writing – review & editing, Supervision, Funding acquisition.

Declaration of competing interest

The authors declare that they have no known competing financial interests or personal relationships that could have appeared to influence the work reported in this paper.

Acknowledgements

C. B. Larsen is supported by the Danish National Committee for Research Infrastructure through DanScatt Grant No. 7129-00006B. S. Samothrakitis is supported through a Swiss Data Science Center LSI Track Grant (Project No. C20-14). The authors would like to acknowledge Dr. Nikhil Mohanan (École Polytechnique, Institut Polytechnique

de Paris) for his help with the EVPFFT simulations. Additionally, the authors would like to thank Dr. Gregory Gerstein and Prof. Dr. Hans Jürgen Maier (Leibniz University Hannover) for the sample preparation. Finally, the authors acknowledge Dr. Tomasz Kacprzak (PSI Center for Scientific Computing, Theory and Data) for his help with the spot segmentation algorithm.

Appendix A. Supplementary data

Supplementary material related to this article can be found online at https://doi.org/10.1016/j.actamat.2025.120869.

References

[1] F.N. Rhines, K.R. Craig, D.A. Rousse, Measurement of average grain volume and certain topological parameters by serial section analysis, Met. Trans. A 7 (1976) 1729–1734.
[2] M.V. Kral, M.A. Mangan, G. Spanos, R.O. Rosenberg, Three-dimensional analysis of microstructures, Mater. Charact. 45 (2000) 17–23.
[3] N. Zaafarani, D. Raabe, R.N. Singh, F. Roters, S. Zaefferer, Three-dimensional investigation of the texture and microstructure below a nanoindent in a Cu single crystal using 3D EBSD and crystal plasticity finite element simulations, Acta Mater. 54 (2006) 1863–1876.
[4] S. Zaefferer, S.I. Wright, D. Raabe, Three-dimensional orientation microscopy in a focused ion beam–scanning electron microscope: A new dimension of microstructure characterization, Met. Mater. Trans. A 39 (2008) 374–389.
[5] F.X. Lin, A. Godfrey, D.J. Jensen, G. Winther, 3D EBSD characterization of deformation structures in commercial purity aluminum, Mater. Charact. 61 (2010) 1203–1210.
[6] H.H. Liu, S. Schmidt, H.F. Poulsen, A. Godfrey, Z.Q. Liu, J.A. Sharon, X. Huang, Three-dimensional orientation mapping in the transmission electron microscope, Science 332 (2011) 833–834.
[7] J. Kopeček, J. Staněk, S. Habr, F. Seitl, L. Petrich, V. Schmidt, V. Beneš, Analysis of Polycrystalline Microstructure of AlMgSc Alloy Observed by 3D EBSD, Image Anal. Ster. 39 (2020) 1–11.
[8] H.F. Poulsen, S.F. Nielsen, E.M. Lauridsen, S. Schmidt, R.M. Suter, U. Lienert, L. Margulies, T. Lorentzen, D. Juul Jensen, Three-dimensional maps of grain boundaries and the stress state of individual grains in polycrystals and powders, J. Appl. Crystallogr. 34 (2001) 751–756.
[9] H.F. Poulsen, Three-dimensional X-ray diffraction microscopy: mapping polycrystals and their dynamics, 2004.
[10] D.J. Jensen, E.M. Lauridsen, L. Margulies, H.F. Poulsen, S. Schmidt, H.O. Sørensen, G.B.M. Vaughan, X-ray microscopy in four dimensions, Mater. Today 9 (2006) 18–25.
[11] W. Ludwig, S. Schmidt, E.M. Lauridsen, H.F. Poulsen, X-ray diffraction contrast tomography: a novel technique for three-dimensional grain mapping of polycrystals. I. Direct beam case, J. Appl. Crystallogr. 41 (2008) 302–309.
[12] G. Johnson, A. King, M.G. Honnicke, J. Marrow, W. Ludwig, X-ray diffraction contrast tomography: a novel technique for three-dimensional grain mapping of polycrystals. II. The combined case, J. Appl. Crystallogr. 41 (2008) 310–318.
[13] W. Ludwig, A. King, P. Reischig, M. Herbig, E.M. Lauridsen, S. Schmidt, H. Proudhon, S. Forest, P. Cloetens, S.R. Du Roscoat, et al., New opportunities for 3D materials science of polycrystalline materials at the micrometre lengthscale by combined use of X-ray diffraction and X-ray imaging, Mater. Sci. Eng.: A 524 (2009a) 69–76.
[14] W. Ludwig, P. Reischig, A. King, M. Herbig, E. Lauridsen, G. Johnson, T.J. Marrow, J.-Y. Buffiere, Three-dimensional grain mapping by x-ray diffraction contrast tomography and the use of Friedel pairs in diffraction data analysis, Rev. Sci. Instrum. 80 (2009).
[15] U. Lienert, S.F. Li, C.M. Hefferan, J. Lind, R.M. Suter, J.V. Bernier, N.R. Barton, M.C. Brandes, M.J. Mills, M.P. Miller, et al., High-energy diffraction microscopy at the advanced photon source, Jom 63 (2011) 70–77.
[16] D.J. Jensen, H.F. Poulsen, The three dimensional X-ray diffraction technique, Mater. Charact. 72 (2012) 1–7.
[17] A. King, P. Reischig, J. Adrien, W. Ludwig, First laboratory X-ray diffraction contrast tomography for grain mapping of polycrystals, J. Appl. Crystallogr. 46 (2013) 1734–1740.
[18] S.A. McDonald, P. Reischig, C. Holzner, E.M. Lauridsen, P.J. Withers, A.P. Merkle, M. Feser, Non-destructive mapping of grain orientations in 3D by laboratory X-ray microscopy, Sci. Rep. 5 (2015) 14665.
[19] B.C. Larson, W. Yang, G.E. Ice, J.D. Budai, J.Z. Tischler, Three-dimensional X-ray structural microscopy with submicrometre resolution, Nature 415 (2002) 887–890.
[20] B.C. Larson, L.E. Levine, Submicrometre-resolution polychromatic three-dimensional X-ray microscopy, J. Appl. Crystallogr. 46 (2013) 153–164.
[21] Y. Zhang, R.I. Barabash, High resolution mapping of orientation and strain gradients in metals by synchrotron 3D X-ray Laue microdiffraction, Quantum Beam Sci. 3 (2019) 6.
[22] J. Oddershede, S. Schmidt, H.F. Poulsen, H.O. Sørensen, J. Wright, W. Reimers, Determining grain resolved stresses in polycrystalline materials using three-dimensional X-ray diffraction, J. Appl. Crystallogr. 43 (2010) 539–549.
[23] P. Reischig, A. King, L. Nervo, N. Viganó, Y. Guilhem, W.J. Palenstijn, K.J. Batenburg, M. Preuss, W. Ludwig, Advances in X-ray diffraction contrast tomography: flexibility in the setup geometry and application to multiphase materials, J. Appl. Crystallogr. 46 (2013) 297–311.
[24] M. Ferry, M.Z. Quadir, N. Afrin, W. Xu, A. Loeb, B. Soe, C. McMahon, C. George, L. Bassman, Uncovering the true nature of deformation microstructures using 3D analysis methods, IOP Conf. Series: Mater. Sci. Eng. 89 (2015) 012002.
[25] P. Sedmák, J. Pilch, L. Heller, J. Kopeček, J. Wright, P. Sedlák, M. Frost, P. Šittner, Grain-resolved analysis of localized deformation in nickel-titanium wire under tensile load, Science 353 (2016) 559–562.
[26] Y. Hayashi, D. Setoyama, Y. Seno, Scanning three-dimensional X-ray diffraction microscopy with a high-energy microbeam at SPring-8, in: Mechanical Stress Evaluation By Neutrons and Synchrotron Radiation VIII, in: Materials Science Forum, vol. 905, Trans Tech Publications Ltd, 2017, pp. 157–164, http://dx.doi.org/10.4028/www.scientific.net/MSF.905.157.
[27] J. Hektor, S.A. Hall, N.A. Henningsson, J. Engqvist, M. Ristinmaa, F. Lenrick, J.P. Wright, Scanning 3DXRD measurement of Grain Growth, Stress, and Formation of Cu_6Sn_5 around a Tin Whisker during heat treatment, Materials 12 (2019).
[28] S. Peetermans, E.H. Lehmann, Simultaneous neutron transmission and diffraction contrast tomography as a non-destructive 3D method for bulk single crystal quality investigations, J. Appl. Phys. 114 (2013).
[29] S. Peetermans, A. King, W. Ludwig, P. Reischig, E.H. Lehmann, Cold neutron diffraction contrast tomography of polycrystalline material, Analyst 139 (2014) 5765–5771.
[30] R. Woracek, D. Penumadu, N. Kardjilov, A. Hilger, M. Boin, J. Banhart, I. Manke, 3D mapping of crystallographic phase distribution using energy-selective neutron tomography, Adv. Mater. 26 (2014) 4069–4073.
[31] A. Cereser, M. Strobl, S.A. Hall, A. Steuwer, R. Kiyanagi, A.S. Tremsin, E.B. Knudsen, T. Shinohara, P.K. Willendrup, A.B. da Silva Fanta, et al., Time-of-flight three dimensional neutron diffraction in transmission mode for mapping crystal grain structures, Sci. Rep. 7 (2017) 9561.
[32] R. Woracek, J. Santisteban, A. Fedrigo, M. Strobl, Diffraction in neutron imaging — A review, Nucl. Instrum. Methods Phys. Res. Sect. A: Accel. Spectrometers, Detect. Assoc. Equip. 878 (2018) 141–158.
[33] M. Raventós, M. Tovar, M. Medarde, T. Shang, M. Strobl, S. Samothrakitis, E. Pomjakushina, C. Grünzweig, S. Schmidt, Laue three dimensional neutron diffraction, Sci. Rep. 9 (2019) 4798.
[34] S. Samothrakitis, M. Raventós, J. Čapek, C.B. Larsen, C. Grünzweig, M. Tovar, M. Garcia-Gonzalez, J. Kopeček, S. Schmidt, M. Strobl, Grain morphology reconstruction of crystalline materials from Laue three-dimensional neutron diffraction tomography, Sci. Rep. 10 (2020) 1–7.
[35] S. Samothrakitis, C.B. Larsen, J. Čapek, E. Polatidis, M. Raventos, M. Tovar, S. Schmidt, M. Strobl, Microstructural characterization through grain orientation mapping with Laue three-dimensional neutron diffraction tomography, Mater. Today Adv. 15 (2022) 100258.
[36] C. Calhoun, E. Garlea, R. Mulay, T. Sisneros, S. Agnew, Investigation of the effect of thermal residual stresses on deformation of α-uranium through neutron diffraction measurements and crystal plasticity modeling, Acta Mater. 85 (2015) 168–179, http://dx.doi.org/10.1016/j.actamat.2014.11.007, URL: https://www.sciencedirect.com/science/article/pii/S1359645414008519.
[37] D.W. Brown, D.P. Adams, L. Balogh, J.S. Carpenter, B. Clausen, G. King, B. Reedlunn, T.A. Palmer, M.C. Maguire, S.C. Vogel, In situ neutron diffraction study of the influence of microstructure on the mechanical response of additively manufactured 304L stainless steel, Met. Mater. Trans. A 48 (2017) 6055–6069, http://dx.doi.org/10.1007/s11661-017-4330-4.
[38] G. Song, Z. Sun, L. Li, B. Clausen, S.Y. Zhang, Y. Gao, P.K. Liaw, High temperature deformation mechanism in hierarchical and single precipitate strengthened ferritic alloys by in situ neutron diffraction studies, Sci. Rep. 7 (2017) 45965, http://dx.doi.org/10.1038/srep45965.
[39] M. Wuttig, J. Li, C. Craciunescu, A new ferromagnetic shape memory alloy system, Scr. Mater. 44 (2001) 2393–2397.
[40] S. Tavares, K. Yang, M.A. Meyers, Heusler alloys: Past, properties, new alloys, and prospects, Prog. Mater. Sci. (2022) 101017.
[41] E. Dogan, I. Karaman, Y.I. Chumlyakov, Z.P. Luo, Microstructure and martensitic transformation characteristics of CoNiGa high temperature shape memory alloys, Acta Mater. 59 (2011) 1168–1183.
[42] T. Niendorf, P. Krooß, C. Somsen, G. Eggeler, Y.I. Chumlyakov, H.J. Maier, Martensite aging–Avenue to new high temperature shape memory alloys, Acta Mater. 89 (2015) 298–304.
[43] J. Liu, H. Xie, Y. Huo, H. Zheng, J. Li, Microstructure evolution in CoNiGa shape memory alloys, J. Alloys Compd. 420 (2006) 145–157.
[44] K. Prusik, B. Kostrubiec, T. Goryczka, G. Dercz, P. Ochin, H. Morawiec, Effect of composition and heat treatment on the martensitic transformations in Co–Ni–Ga alloys, Mater. Sci. Engineering: A 481 (2008) 330–333.
[45] M.A. Amin, N. El-Bagoury, M.H.H. Mahmoud, M.M. Hessien, S.S. Abd El-Rehim, J. Wysocka, J. Ryl, Catalytic impact of alloyed Al on the corrosion behavior of $Co_{50}Ni_{23}Ga_{26}Al_{1.0}$ magnetic shape memory alloy and catalysis applications for efficient electrochemical H_2 generation, RSC Adv. 7 (2017) 3635–3649.

[46] S. Samothrakitis, C.B. Larsen, R. Woracek, L. Heller, J. Kopeček, G. Gerstein, H.J. Maier, M. Rameš, M. Tovar, P. Šittner, et al., A multiscale study of hot-extruded CoNiGa ferromagnetic shape-memory alloys, Mater. Des. 196 (2020) 109118.
[47] J. Dadda, H.J. Maier, D. Niklasch, I. Karaman, H.E. Karaca, Y.I. Chumlyakov, Pseudoelasticity and cyclic stability in $Co_{49}Ni_{21}Ga_{30}$ shape-memory alloy single crystals at ambient temperature, Met. Mater. Trans. A 39 (2008) 2026–2039.
[48] P. Krooß, T. Niendorf, P.M. Kadletz, C. Somsen, M.J. Gutmann, Y.I. Chumlyakov, W.W. Schmahl, G. Eggeler, H.J. Maier, Functional fatigue and tension–compression asymmetry in [001]-oriented $Co_{49}Ni_{21}Ga_{30}$ high-temperature shape memory alloy single crystals, Shape Mem. Superelasticity 1 (2015) 6–17.
[49] M. Vollmer, P. Krooß, C. Segel, A. Weidner, A. Paulsen, J. Frenzel, M. Schaper, G. Eggeler, H.J. Maier, T. Niendorf, Damage evolution in pseudoelastic polycrystalline Co–Ni–Ga high-temperature shape memory alloys, J. Alloys Compd. 633 (2015) 288–295.
[50] A. Reul, C. Lauhoff, P. Krooß, M.J. Gutmann, P.M. Kadletz, Y.I. Chumlyakov, T. Niendorf, W.W. Schmahl, In situ neutron diffraction analyzing stress-induced phase transformation and martensite elasticity in [001]-oriented $Co_{49}Ni_{21}Ga_{30}$ shape memory alloy single crystals, Shape Mem. Superelasticity 4 (2018) 61–69.
[51] C. Lauhoff, M. Vollmer, P. Krooß, I. Kireeva, Y.I. Chumlyakov, T. Niendorf, Pathways towards grain boundary engineering for improved structural performance in polycrystalline Co–Ni–Ga shape memory alloys, Shape Mem. Superelasticity 5 (2019) 73–83.
[52] C. Lauhoff, N. Sommer, M. Vollmer, G. Mienert, P. Krooß, S. Böhm, T. Niendorf, Excellent superelasticity in a Co-Ni-Ga high-temperature shape memory alloy processed by directed energy deposition, Mater. Res. Lett. 8 (2020) 314–320.
[53] C. Lauhoff, T. Pham, A. Paulsen, P. Krooß, J. Frenzel, G. Eggeler, T. Niendorf, A novel thermo-mechanical processing route exploiting abnormal grain growth in Heusler-type Co–Ni–Ga shape memory alloys, Met. Mater. Trans. A 53 (2022) 4139–4142.
[54] E. Karsten, G. Gerstein, O. Golovko, A. Dalinger, C. Lauhoff, P. Krooss, T. Niendorf, A. Samsonenko, H.J. Maier, Tailoring the microstructure in polycrystalline Co–Ni–Ga high-temperature shape memory alloys by hot extrusion, Shape Mem. Superelasticity 5 (2019) 84–94.
[55] T. Niendorf, C. Lauhoff, E. Karsten, G. Gerstein, A. Liehr, P. Krooß, H.J. Maier, Direct microstructure design by hot extrusion–high-temperature shape memory alloys with bamboo-like microstructure, Scr. Mater. 162 (2019) 127–131.
[56] R.A. Lebensohn, A.K. Kanjarla, P. Eisenlohr, An elasto-viscoplastic formulation based on fast Fourier transforms for the prediction of micromechanical fields in polycrystalline materials, Int. J. Plast. 32-33 (2012) 59–69.
[57] M. Upadhyay, S. Van Petegem, T. Panzner, R. Lebensohn, H. Van Swygenhoven, Study of lattice strain evolution during biaxial deformation of stainless steel using a finite element and fast Fourier transform based multi-scale approach, Acta Mater. 118 (2016) 28–43.
[58] G.N. Iles, S. Schorr, The HZB neutron Laue diffractometer: From E11 to FALCON, Neutron News 25 (2014) 27–29.
[59] S. Samothrakitis, C.B. Larsen, A. Kaestner, E. Polatidis, J. Čapek, J. Hovind, A. Fazan, J. Allibon, M. Busi, S. Schmidt, et al., The FALCON double-detector Laue diffractometer add-on for grain mapping at POLDI, J. Appl. Crystallogr. 56 (2023).
[60] R. Woracek, D. Penumadu, N. Kardjilov, A. Hilger, M. Strobl, R.C. Wimpory, I. Manke, J. Banhart, Neutron Bragg-edge-imaging for strain mapping under in situ tensile loading, J. Appl. Phys. 109 (2011) 093506.
[61] P.J. Brown, K. Ishida, R. Kainuma, T. Kanomata, K.U. Neumann, K. Oikawa, B. Ouladdiaf, K.R.A. Ziebeck, Crystal structures and phase transitions in ferromagnetic shape memory alloys based on Co-Ni-Al and Co-Ni-Ga, J. Phys.: Condens. Matter. 17 (2005) 1301.
[62] R. Geda, S.M. Crawford, L. Hunt, M. Bershady, E. Tollerud, S. Randriamampandry, PetroFit: A Python package for computing petrosian radii and fitting galaxy light profiles, Astron. J. 163 (2022) 202.
[63] L. Bradley, B. Sipőcz, T. Robitaille, E. Tollerud, Z. Vinícius, C. Deil, K. Barbary, T.J. Wilson, I. Busko, A. Donath, H.M. Günther, M. Cara, P.L. Lim, S. Meßlinger, S. Conseil, A. Bostroem, M. Droettboom, E.M. Bray, L.A. Bratholm, G. Barentsen, M. Craig, S. Rathi, S. Pascual, G. Perren, I.Y. Georgiev, M. de Val-Borro, W. Kerzendorf, Y.P. Bach, B. Quint, H. Souchereau, astropy/photutils: 1.5.0, 2022, http://dx.doi.org/10.5281/zenodo.6825092.
[64] J.J. Wortman, R.A. Evans, Young's modulus, shear modulus, and Poisson's ratio in silicon and germanium, J. Appl. Phys. 36 (1965) 153–156.
[65] L. Zhang, R. Barrett, P. Cloetens, C. Detlefs, M. Sanchez del Rio, Anisotropic elasticity of silicon and its application to the modelling of X-ray optics, J. Synchrotron Radiat. 21 (2014) 507–517.
[66] J. Bai, D. Liu, R. Huang, Z. Zhang, Y. Yang, J. Gu, H. Yan, X. Zhao, L. Zuo, Phase stability, magnetic and elastic properties of Co_2NiGa alloy: A first-principles calculation, Mater. Today Commun. 22 (2020) 100810.
[67] J. Michel, H. Moulinec, P. Suquet, A computational method based on augmented lagrangians and fast fourier transforms for composites with high contrast, CMES(Comput. Model. Eng. Sci.) 1 (2000) 79–88.
[68] A. Lindkvist, Y. Zhang, Three-dimensional grain resolved strain mapping using laboratory X-ray diffraction contrast tomography: theoretical analysis, J. Appl. Crystallogr. 55 (2022) 21–32.
[69] B.D. Fu, K. Du, G.M. Han, C.Y. Cui, J.X. Zhang, Deformation mechanisms in a Co-rich nickel based superalloy with different size of γ precipitates, Mater. Lett. 152 (2015) 272–275.